

**Momentum mapping of continuum-electron wave-packet interference**Weifeng Yang,<sup>1</sup> Huatang Zhang,<sup>1</sup> Cheng Lin,<sup>1</sup> Jingwen Xu,<sup>1</sup> Zhihao Sheng,<sup>1</sup> Xiaohong Song,<sup>1,\*</sup> Shilin Hu,<sup>2,3</sup> and Jing Chen<sup>2,3,†</sup><sup>1</sup>*Department of Physics, College of Science, Shantou University, Shantou, Guangdong 515063, China*<sup>2</sup>*CAPT, HEDPS, and IFSA Collaborative Innovation Center of MoE, College of Engineering, Peking University, Beijing 100084, China*<sup>3</sup>*Institute of Applied Physics and Computational Mathematics, P.O. Box 8009, Beijing 100088, China*

(Received 28 June 2016; published 21 October 2016)

We analyze the two-dimensional photoelectron momentum distribution of an Ar atom ionized by midinfrared laser pulses and mainly concentrate on the energy range below  $2U_p$ . By using a generalized quantum trajectory Monte Carlo simulation and comparing with the numerical solution of the time-dependent Schrödinger equation, we demonstrate that a profound ringlike pattern coming from the interplay between the intra- and the intercycle interferences of electron trajectories can be observed in the deep tunneling ionization regime. Moreover, we found that the rescattered electrons play a negligible role on the formation of a ringlike interference pattern, and the appearance of the ringlike interference pattern masks the holographic interference structure. Our results provide an appropriate experimental condition for the observation of the photoelectron holography and help to gain physical insight into the corresponding ultrafast electron dynamic process with attosecond temporal resolution.

DOI: [10.1103/PhysRevA.94.043419](https://doi.org/10.1103/PhysRevA.94.043419)**I. INTRODUCTION**

Atomic photoionization under intense laser irradiation is a fundamental process in strong-field light-matter interaction. The physical picture is understood by the simple man's model [1]. Within this model, the electron is released first from its parent atomic core, then is accelerated in the laser field and redirected to the parent ion, and finally recollides with the parent ion. Usually, the ionization process is divided into two regimes: multiphoton ionization and tunneling ionization. The Keldysh parameter  $\gamma = \sqrt{\frac{I_p}{2U_p}}$  ( $I_p$  is the ionization potential, and  $U_p = \frac{I}{4\omega^2}$  denotes the ponderomotive energy, where  $I$  is the laser intensity and  $\omega$  is the angular frequency) is an indicator as to distinguish these two ionization regimes [2]. When  $\gamma$  is much less than 1, the ionization process is in the tunneling regime where quasistatic approximation is valid. When  $\gamma$  is much larger than 1, it is in the multiphoton ionization regime. When  $\gamma \sim 1$ , it is considered to be a transition from the tunneling regime to the multiphoton regime, and the barrier in the combined Coulomb and laser field potentials changes significantly during tunneling [3].

Interference is a very important concept of coherent matter waves which has been extended successfully to explore highly nonlinear quantum-mechanical phenomena in strong-field light-matter interaction. The interference of the two electron wave packets (EWPs) ionized with exactly one optical cycle relative delay reaching the same final momentum gives rise to above-threshold ionization (ATI) rings, i.e., the intercycle interference, that are spaced by the energy of one photon in the photoelectron spectrum. In addition to the intercycle interference, a temporal double-slit pattern can be verified as the signature of EWP interference emitted from the successive maxima of the absolute value of the electric field, which is the intracycle interference [4,5]. The interference pattern of the interplay between intra- and intercycle interferences

in photoelectron spectra has been identified as a diffraction pattern for a time grating [5–9]. Recently, a holographic structure has been observed in photoionization, and it is demonstrated to be the interference between the direct and the rescattered EWPs ionized within the same quarter cycle of the laser pulse [10–15]. All these interference processes interplay with each other, and various interference patterns will mix together in the photoelectron spectrum. As a result, establishing an unambiguous one-to-one relationship between a certain interference pattern and the corresponding electronic dynamic process is essential for retrieving the information of electronic dynamics from the measured photoelectron momentum spectrum.

On the other hand, with the development of intense midinfrared (mid-IR) sources, experimental probing deep into the tunneling regime has become possible. Using a high repetition rate optical parametric chirped pulse amplifier, Keldysh parameters approaching  $\gamma \sim 0.1$  can be achieved [16]. In this regime, an unexpected low-energy structure, a very low-energy structure, and even a zero-energy structure have been observed [17–21]. All these experimental results and the following theoretical analysis greatly advance people's understanding in this field. In the original paper of strong-field photoelectron holography, tunneling ionization had been assumed to be essential for the holographic interference (in that experiment,  $\gamma = 0.76$ ) [10]. Subsequently, investigations indicated that the holographic interference pattern can also be observed under the conditions that belong to the multiphoton regime ( $\gamma > 1$ ) [11]. However, whether the photoelectron hologram can be observed in the deep tunneling regime (i.e.,  $\gamma \ll 1$ ) is analyzed here.

In the present paper, we analyze the photoelectron angular distributions (PADs) in atomic ATI with midinfrared laser pulses. A profound ringlike interference pattern is identified by both the time-dependent Schrödinger equation (TDSE) and the generalized quantum-trajectory Monte Carlo (GQTMC) simulations in the deep tunneling regime. Within the description of the GQTMC, the ringlike interference pattern is demonstrated to be the superposition between the intra- and the intercycle interferences. The center of the ringlike interference

\*songxh@stu.edu.cn

†chen\_jing@iapcm.ac.cn

pattern lies in where separations between adjacent temporal double-slit interference fringes are nearly the same as those of the ATI rings. Moreover, the Coulomb potential plays a negligible role in the formation of the ringlike interference pattern. The ringlike interference pattern masks the holographic interference pattern in the low final longitudinal momentum range so that the holographic interference pattern can only be observed in the high final longitudinal momentum range. As a result, we identify that deep tunneling is not an appropriate condition for observing the holographic interference pattern. In the nonadiabatic tunneling regime, the contribution of the rescattering electron trajectories will increase, so the holographic interference will clearly be observed.

This paper is organized as follows. In Sec. II we introduce the theoretical methods including the numerical solutions of the TDSE and the GQTMC models. In Sec. III, first, we show different characteristics of the interference structures in PADs with different midinfrared laser pulses using the TDSE and GQTMC simulations. Second, the underlying mechanism of the ringlike pattern is discussed based on the GQTMC statistical trajectory-based analysis. Moreover, the intra- and intercycle interferences and the Coulomb potential effects on the interference pattern are discussed. We summarize our results and conclude in Sec. IV.

## II. THEORETICAL MODELS

In this section, we summarize the numerical solution of the TDSE and the GQTMC methods. The numerical solution of the TDSE can be used as a benchmark for assessing the validity of the GQTMC simulation.

### A. The numerical solution of the time-dependent Schrödinger equation

We consider an Ar atom interacting with a linearly polarized laser field. The electric field of the laser pulse is

$$\mathbf{E}(t) = E_0 f(t) \cos(\omega t) \hat{z}, \quad (1)$$

where  $\hat{z}$  is the laser polarization direction with  $f(t)$  as the pulse envelope function.  $E_0$  is the peak field strength. Numerical solutions of the TDSE within the single-active-electron (SAE) approximation have been shown to yield good agreement with experimental results in Ar atoms for an extremely wide laser parameters [17,22,23]. The TDSE within the SAE approximation is

$$i \frac{\partial}{\partial t} \Psi(\mathbf{r}, t) = \left\{ \frac{\mathbf{p}^2}{2} + \mathbf{p} \cdot \mathbf{A}(t) + \mathbf{V}(\mathbf{r}) \right\} \Psi(\mathbf{r}, t). \quad (2)$$

Here,  $\mathbf{r}$  and  $\mathbf{p}$  are the position and the momentum of the electron,  $\mathbf{V}(\mathbf{r})$  is the atomic potential of Ar, and  $\mathbf{A}(t) = -\int_0^t \mathbf{E}(t') dt'$  is the vector potential, respectively. The time evolution of the wave-function  $\Psi(t)$  is evaluated by using the split-operation method in the energy representation [24–26]. The space is split into two parts, i.e., the inner and outer regions where the atomic potential becomes negligible compared to the kinetic energy. When the time-dependent wave function in space reaches the outer region, we project the outer region wave function on Volkov states to obtain the PAD [13,27].

The initial ground state is obtained by the imaginary time-propagation method.

### B. The generalized quantum trajectory Monte Carlo method

To explore the physical reason for the TDSE results, we apply a GQTMC method [15] based on the nonadiabatic ionization theory [28,29], classical dynamics with combined laser and Coulomb fields [30–33], and Feynman's path-integral approach [34,35]. The ionization rate is given as

$$\Gamma(t) = N(t) \exp\left(-\frac{E_0^2 f^2(t)}{\omega^3} \Phi(\gamma(t), \theta(t))\right), \quad (3)$$

where  $\theta(t)$  is the phase of the laser electric field. The function  $\Phi(\gamma, \theta)$  is given by the following expression [28]:

$$\begin{aligned} \Phi(\gamma, \theta) &= \left( \gamma^2 + \sin^2 \theta + \frac{1}{2} \right) \ln c - \frac{3\sqrt{b-a}}{2\sqrt{2}} \sin |\theta| \\ &\quad - \frac{\sqrt{b+a}}{2\sqrt{2}} \gamma, \\ a &= 1 + \gamma^2 - \sin^2 \theta, \\ b &= \sqrt{a^2 + 4\gamma^2 \sin^2 \theta}, \\ c &= \sqrt{\left( \frac{\sqrt{b+a}}{2} + \gamma \right)^2 + \left( \frac{\sqrt{b-a}}{2} + \sin |\theta| \right)^2}. \end{aligned} \quad (4)$$

For convenience of analysis, the laser pulse envelope  $f(t)$  is half-trapezoidal, constant for the first four cycles, and ramped off linearly within the last two cycles. The preexponential factor is

$$\begin{aligned} N(t) &= A_{n^*, l^*} B_{l, |m|} \left( \frac{3\kappa}{\gamma^3} \right)^{1/2} C I_p \left( \frac{2(2I_p)^{3/2}}{E(t)} \right)^{2n^* - |m| - 1} \\ \kappa &= \ln(\gamma + \sqrt{\gamma^2 + 1}) - \frac{\gamma}{\sqrt{\gamma^2 + 1}}. \end{aligned} \quad (5)$$

Here, the coefficients  $A_{n^*, l^*}$  and  $B_{l, |m|}$  coming from the radial and angular parts of the wave function, are given by Eq. (2) of Ref. [28].  $C = (1 + \gamma^2)^{|m|/2 + 3/4} A_m(\omega, \gamma)$  is the Perelomov-Popov-Terent'ev correction to the quasistatic limit  $\gamma \ll 1$  of the Coulomb preexponential factor with  $A_m$  given by Eqs. (55) and (56) of Ref. [29]. The tunneled electrons have a Gaussian distribution on the initial transverse momentum  $\Omega(v_r^j, t_0) \propto [v_r^j \sqrt{2I_p} / |E(t_0)|] \exp[\sqrt{2I_p} (v_r^j)^2 / |E(t_0)|]$ . The coordinate of the tunnel exit shifts toward the atomic core due to the nonadiabatic effects [29], and the tunnel exit point is

$$Z_0 = \frac{2I_p}{E(t_0)} [1 + \sqrt{1 + \gamma^2(t_0)}]^{-1}. \quad (6)$$

Thereafter, the classical motion of the electrons in the combined laser and Coulomb fields is governed by the Newtonian equation,

$$\frac{d^2}{dt^2} \mathbf{r} = -\mathbf{E}(t) - \nabla(\mathbf{V}(\mathbf{r})). \quad (7)$$

According to Feynman's path-integral approach, the phase of the  $j$ th electron trajectory is given by the classical action along

the trajectory,

$$S_j(\mathbf{p}, t_0) = \int_{t_0}^{+\infty} \{v_{\mathbf{p}}^2(\tau)/2 + I_p - 1/|\mathbf{r}(t)|\} d\tau, \quad (8)$$

where  $\mathbf{p}$  is the asymptotic momentum of the  $j$ th electron trajectory. The probability of each asymptotic momentum is determined by

$$|\Psi_{\mathbf{p}}|^2 = \left| \sum_j \sqrt{\Gamma(t_0, v_r^j)} \exp(-iS_j) \right|^2. \quad (9)$$

In Ref. [15], it has been shown that the GQTMC simulation can reproduce well the experimental result in Ref. [10]. As we will show in the following section, one can also reproduce the TDSE results and extract all the information about the electron trajectory including the initial ionization phase and velocity. Moreover, by the GQTMC method, one can reconstruct the momentum distribution with the photoelectrons from a special subcycle time window, which is in favor of exploring the interference and Coulomb potential effects.

### III. RESULTS AND DISCUSSION

Using the TDSE [Figs. 1(a), 1(c), 1(e), and 1(g)] and the GQTMC [Figs. 1(b), 1(d), 1(f), and 1(h)] simulations, we have calculated PADs of ionization from an Ar atom in linearly polarized laser fields with different laser parameters (1300 nm,  $2.13 \times 10^{14}$  W/cm<sup>2</sup> and 900 nm,  $4.44 \times 10^{14}$  W/cm<sup>2</sup> corresponding to  $\gamma = 0.48$ ,  $0.4 \times 10^{14}$  W/cm<sup>2</sup> and 900 nm,  $0.835 \times 10^{14}$  W/cm<sup>2</sup> corresponding to  $\gamma = 1.12$ ). The GQTMC simulations reproduce well the main features of the TDSE results in both the tunneling ionization and the transition regimes. Both the TDSE and the GQTMC simulations show that, in the tunneling ionization regime,

in addition to the ATI rings which center at zero, another ringlike interference pattern centering at about  $p_z \sim 0.56$  a.u. and  $p_r = 0$  can clearly be observed. However, in the transition regime where  $\gamma \sim 1$ , the ringlike interference pattern disappears, whereas the holographic “fork” interference structure can be identified in the PADs. It is worthwhile mentioning that some differences between the two methods can be found in Fig. 1, for example, the widths of the holographic interference fringes in the GQTMC simulations [Figs. 1(e) and 1(g)] are wider than that in the TDSE results [Figs. 1(f) and 1(h)]. These differences may be attributed to the inaccuracy of the initial conditions of the trajectories in the GQTMC method, e.g., initial longitudinal velocity (which is assumed to be zero in our calculation). Generally speaking, the GQTMC model is an approximation method, however, the agreement between the method and the TDSE calculation is good enough to demonstrate the fact that the PADs would be quite different in different Keldysh parameter regimes. It is noteworthy that these features are dependent on the Keldysh parameter but not the wavelength of the laser field as shown in Fig. 1. Next we will discuss the physical mechanism of the ringlike interference pattern and the conditions required for the appearance of different interference patterns.

With the help of the GQTMC back analysis, we can disentangle contributions of photoelectrons emitted from different time windows and illuminate the interplay among them. We find that the photoelectrons contributing to the ringlike fringes come from at least three subcycle time windows which are labeled A–C in Fig. 2(a). In the time window A or B, there are two kinds of typical trajectories: the rescattered trajectory [trajectory R in Fig. 2(b)] and the so-called indirect trajectory [trajectory ID in Fig. 2(c)]. The main distinction between these two kinds of trajectories lies in that the wave packet of trajectory ID does not interact with the parent ion when it

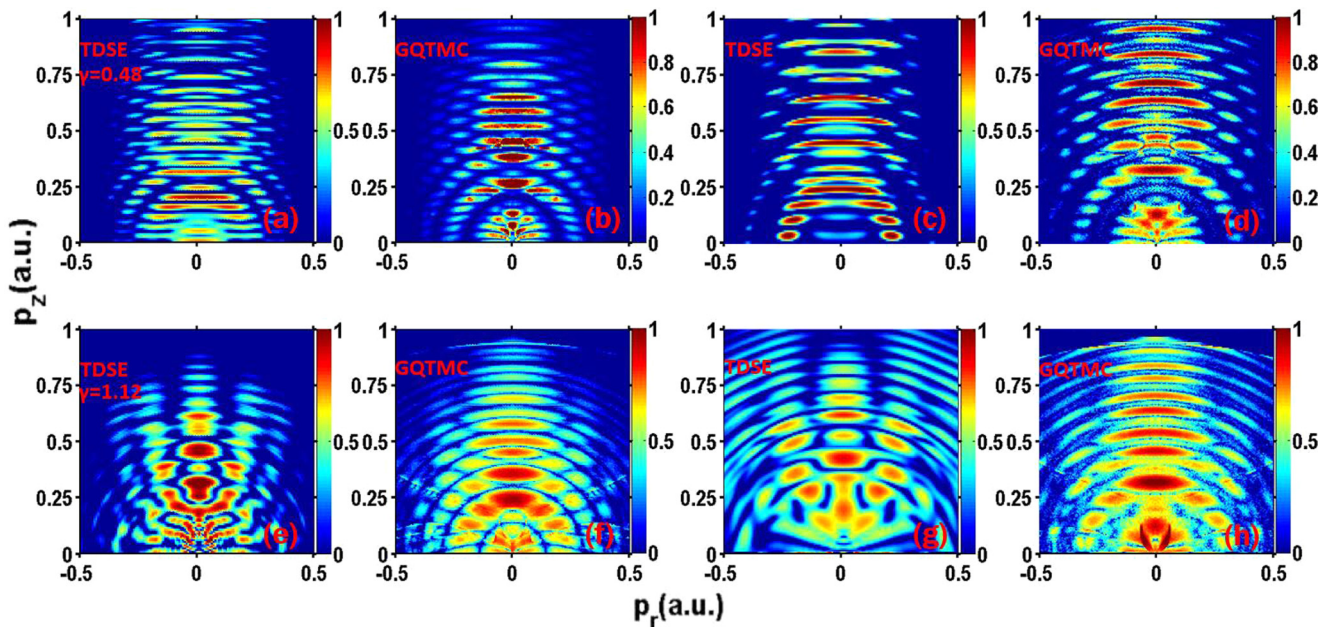


FIG. 1. Simulated two-dimensional (2D) photoelectron momentum spectra of an Ar atom. Upper panel:  $\gamma = 0.48$ , lower panel:  $\gamma = 1.12$ . (a) and (b)  $I = 2.13 \times 10^{14}$  W/cm<sup>2</sup>,  $\lambda = 1300$  nm, (c) and (d)  $4.44 \times 10^{14}$  W/cm<sup>2</sup>,  $\lambda = 900$  nm, (e) and (f)  $I = 0.4 \times 10^{14}$  W/cm<sup>2</sup>,  $\lambda = 1300$  nm, and (g) and (h)  $0.835 \times 10^{14}$  W/cm<sup>2</sup>,  $\lambda = 900$  nm.

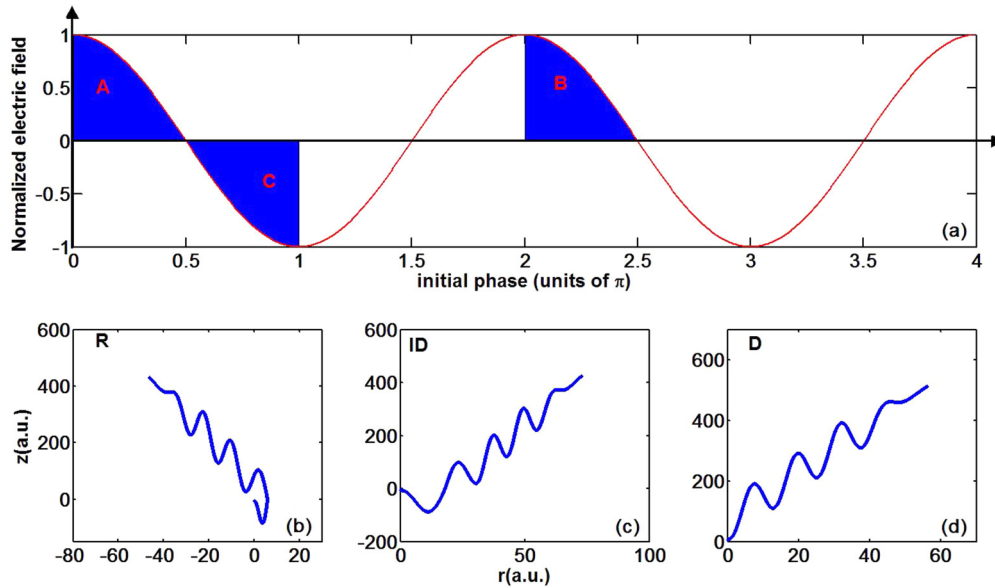


FIG. 2. Upper panel (a): Subcycle time windows from which photoelectrons are emitted. Lower panel: (b) the typical trajectory R, (c) the typical trajectory ID, and (d) the typical trajectory D.

comes back close to  $z = 0$ . The interference between these two types of trajectories from single A or B induces the forklike holographic interference pattern. In window C, there is only one kind of typical trajectory: direct trajectory [trajectory D in Fig. 2(d)]. It has been well known that the intercycle interference of the EWPs liberated with a relative time delay of one optical cycle (for example, the interference between EWPs coming from windows A and B) will induce a series of ATI rings separated by one photon energy. Whereas the intracycle interference of the EWPs from windows A and C induces a temporal double-slit pattern which has been studied both experimentally and theoretically [4].

Figure 3 shows reconstructed photoelectron momentum spectra with EWPs from different time windows. Figures 3(a)

and 3(d) show the temporal double-slit interference pattern reconstructed with EWPs released from time windows A and C; Figs. 3(b) and 3(e) are the ATI interference pattern reconstructed with EWPs from time windows A and B; whereas Figs. 3(c) and 3(f) are photoelectron spectra reconstructed with EWPs released from all three time windows A–C. One can see that, compared with the outgoing ATI rings, the temporal double-slit interference pattern is an incoming structure. Moreover, the separations of neighbor incoming fringes are unequal and, on the contrary to the ATI rings, gradually increase with energy in the momentum distribution map.

To show more clearly the influence of the Coulomb potential, we further present the results without considering

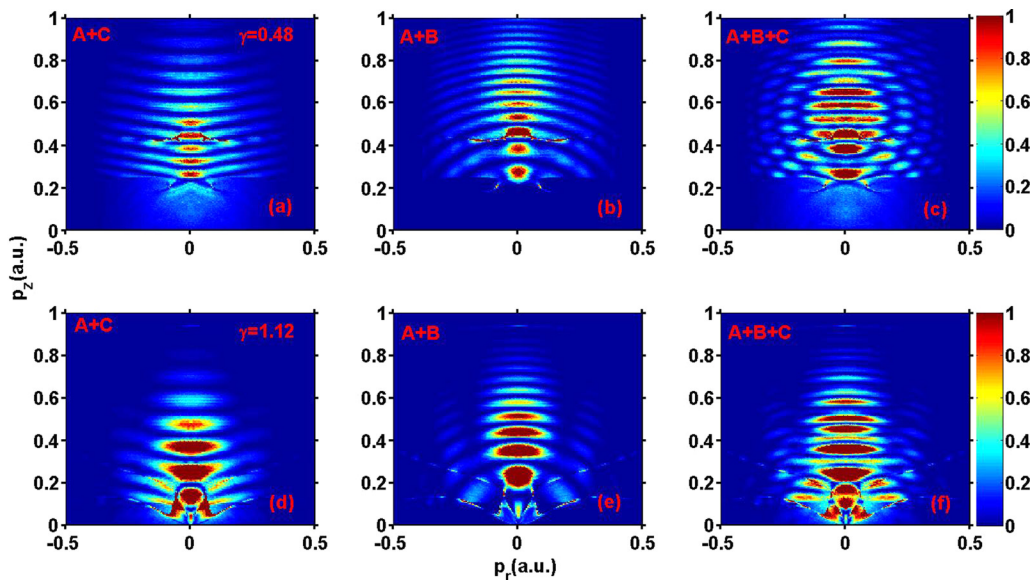


FIG. 3. Reconstructed photoelectron momentum spectra with EWPs from different time windows: (a) and (d) with EWPs from time windows A and B; (b) and (e) from time windows A and C; (c) and (f) from time windows A–C. (a)–(c)  $\gamma = 0.48$ . (d)–(f)  $\gamma = 1.12$ .

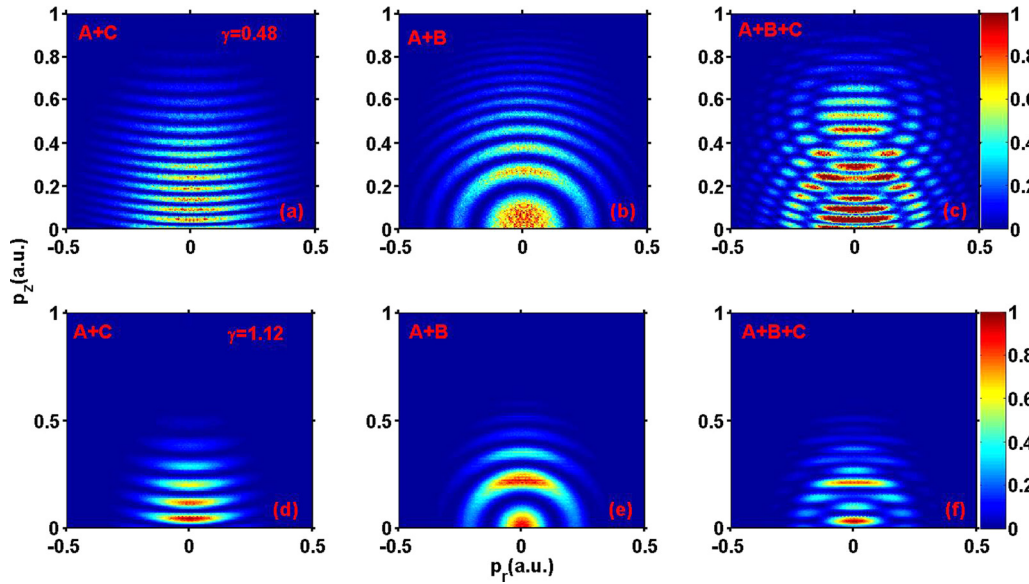


FIG. 4. The same as with Fig. 3 but without considering the Coulomb potential.

the Coulomb potential in Fig. 4. Comparing with Fig. 3, we can see that the impact of the Coulomb potential is reflected mainly in: (i) It distorts substantially the PADs in the low momentum ranges; (ii) it introduces the rescattered trajectory, i.e., trajectory R. Without the Coulomb potential, trajectory R will not exist, and so does the holographic interference. In both Figs. 3(a) and 3(b), the holographic interference structures can hardly be seen, which means that the contribution of trajectory R is quite small under the laser condition  $\gamma = 0.48$ . Most interestingly, when we reconstruct the momentum distribution of photoelectrons from all three windows, the ringlike interference pattern comes out in both

cases with and without considering the Coulomb potential [see Figs. 3(c) and 4(c)], demonstrating that the Coulomb potential and the induced trajectory R play a negligible role in this interference.

In the case of  $\gamma = 1.12$ , the situation is quite different. The contribution of trajectory R can already be discerned in the intracycle temporal double-slit interference structure. In the intercycle interference PAD [see Fig. 3(e)], both the forklike holographic interference pattern along with the ATI rings can clearly be distinguished. Remarkably different from the case of  $\gamma = 0.48$ , the momentum distribution of photoelectrons from these three windows cannot form a ringlike

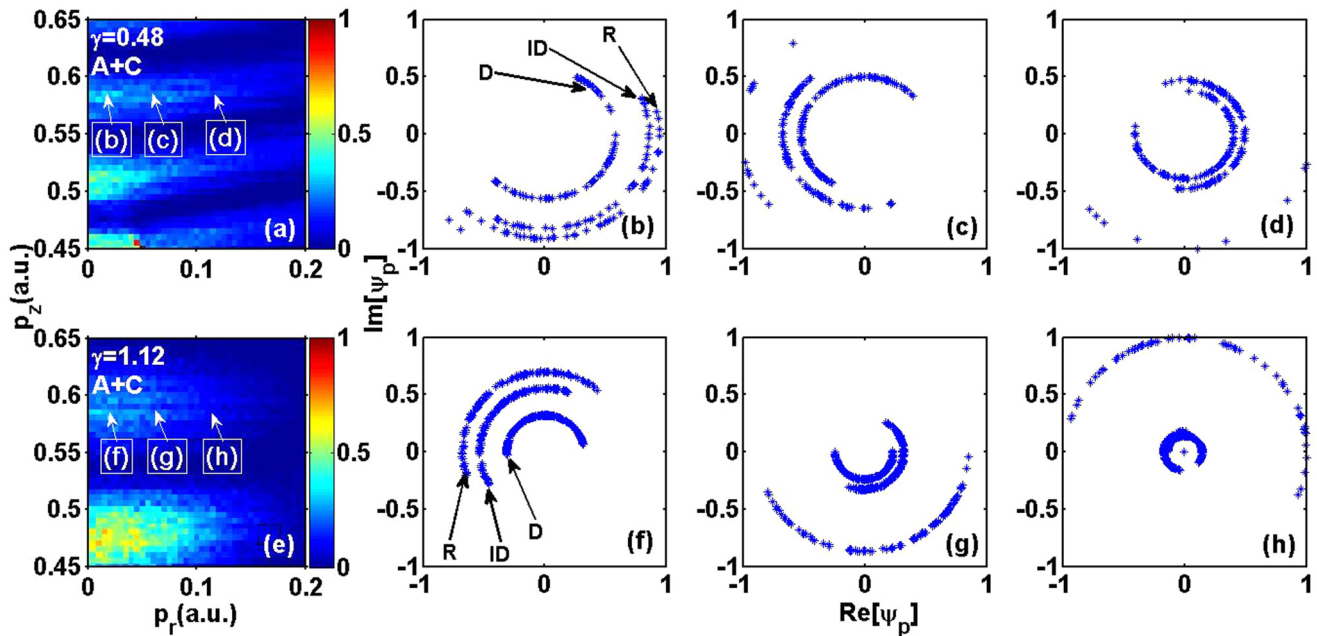


FIG. 5. (a) and (e) present zooms into Figs. 3(a) and 3(d) with three sampling points indicated. (b)–(d) and (f)–(h) show the probabilities of the summed trajectories  $\Psi_p$  on the complex plane.

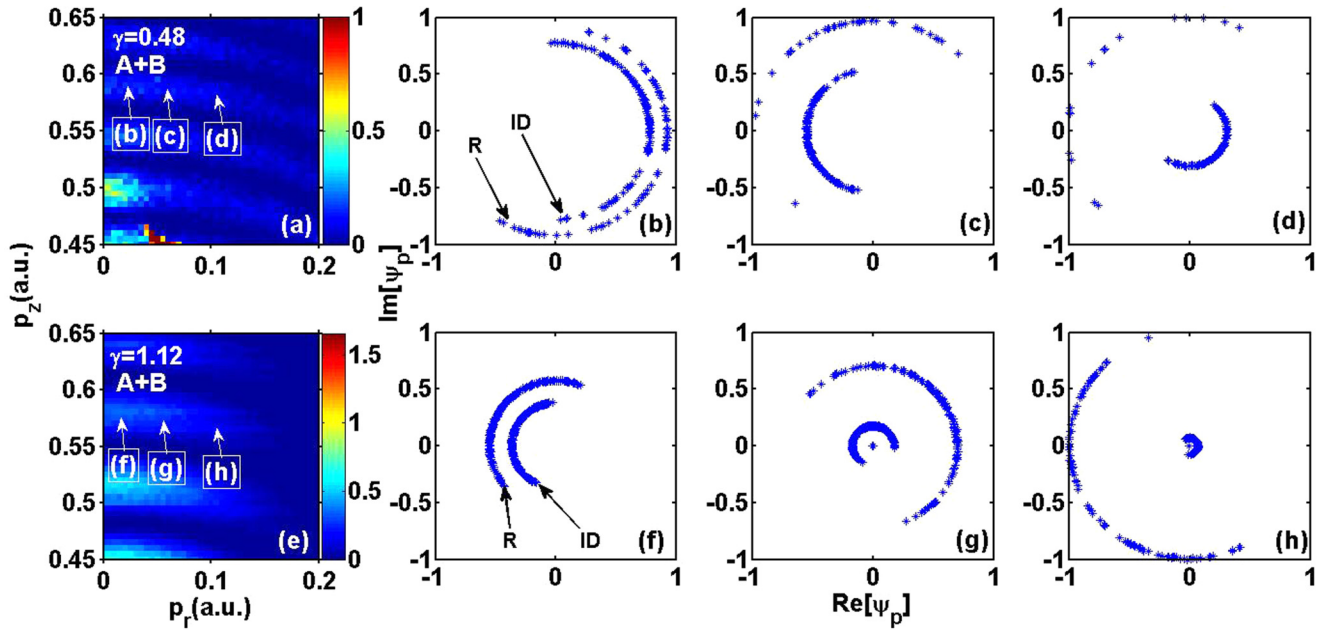
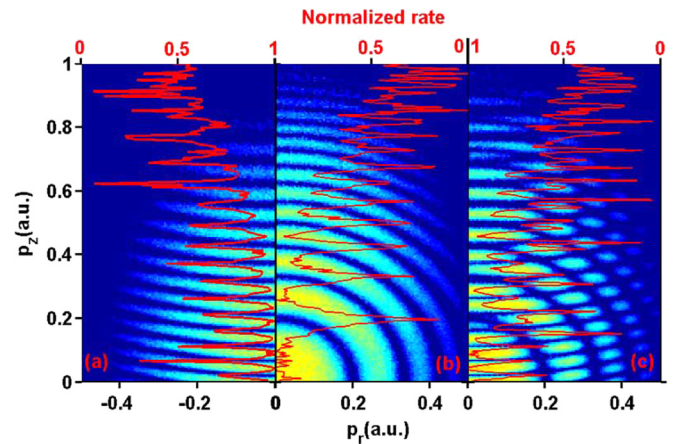


FIG. 6. The same as with Fig. 5 but for three sampling points in Figs. 3(b) and 3(e).

structure. On the contrary, the holographic interference structure can clearly be observed [see Fig. 3(f)]. This demonstrates that the rescattered trajectory R indeed contributes importantly to holographic interference in the total PAD.

The above results can further be demonstrated by the statistical trajectory-based analysis on the complex plane [36]. Figures 5(a) and 5(e) present zooms into Figs. 3(a) and 3(d). Figures 5(b)–5(d) and 5(f)–5(h) show the probabilities of the trajectories  $\Psi_p$  on the complex plane (the radius represents the weight  $|\sqrt{\Gamma(t_0, v_r^T)}|$ , and the angle represents phase  $S_j$  of each trajectory) for the three sampling points indicated in Figs. 5(a) and 5(e), respectively. Figure 6 shows the same analysis but for the intercycle interference [Figs. 3(b) and 3(e)]. It can be seen that, for each sampling point in the intracycle interference pattern, there are three arcs which correspond to the three different kinds of electron trajectories (trajectories D, ID, and R), whereas for intercycle interference, only two arcs corresponding to trajectories ID and R contribute to the interference pattern. The outermost arc corresponds to the rescattered trajectory R. When the two arcs align in the same direction, constructive interference occurs, otherwise, the opposite alignment leads to destructive interference. By comparing the two cases with different laser conditions, we can see that, for  $\gamma = 0.48$ , the number of the rescattered trajectory R is greatly reduced. On the contrary, for  $\gamma = 1.12$ , the rescattered trajectory R contributes greatly to the total momentum spectrum. As a result, the holographic interference structure can clearly be distinguished from the total momentum distribution spectra [see Figs. 1(c) and 1(d)]. All these are consistent with the above analysis. Therefore, we can conclude that the rescattered trajectory R is very vital: When the contribution of rescattered trajectory R increases, the holographic interference pattern will clearly be visible, otherwise, the ringlike interference structure will be formed due to the interplay between the intra- and the intercycle interferences of direct and indirect electron trajectories.

Since the Coulomb potential plays a negligible role in the ringlike interference, to shed more light on its physical origination, the following analysis will be based on the GQTC simulations without considering the Coulomb potential. Figures 7(a)–7(c) show the temporal double-slit interference patterns, ATI rings, and the total momentum distribution spectrum, respectively. The red lines indicate the momentum spectrum for  $p_r = 0$ . We find that at a small momentum range (i.e.,  $p_z < 0.56$  a.u.), the separations between adjacent temporal double-slit interference fringes are smaller than those of the ATI rings. As a result, the total photoelectron spectrum clearly shows the modulation of the intracycle double-slit interference by the intercycle interference. At around  $p_z \sim 0.56$  a.u., the separations between adjacent temporal double-slit interference fringes are nearly the same as those of the ATI rings. In the total momentum distribution


 FIG. 7. (a) The temporal double-slit interference patten, (b) ATI rings, (c) the total momentum distribution reconstructed with EWPs from three time windows A–C. The red lines indicate the momentum spectrum for  $p_r = 0$  a.u.

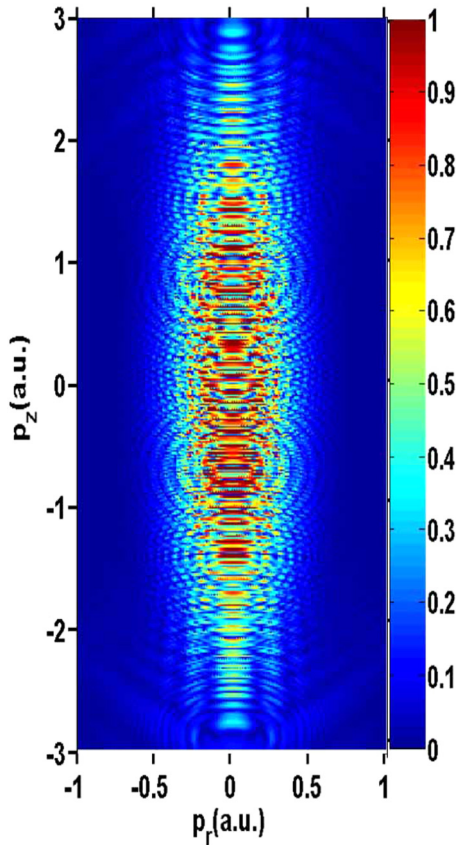


FIG. 8. TDSE simulation in the deep tunneling regime:  $\gamma = 0.28$ ,  $I = 2.76 \times 10^{14}$  W/cm<sup>2</sup>,  $\lambda = 2000$  nm.

spectrum, this forms the center of the ringlike interference pattern. Above this momentum region, the separations of temporal double-slit interference fringes are larger than those of the ATI fringes, so the double-slit interference fringes are imprinted on a modulation envelope of the ATI fringes. We collect the phases of indirect and direct electron trajectories from time windows A–C resulting in the ringlike pattern and found that the phase difference between electron trajectories from A and B is approximately equal to that from A and C, which confirms the above analysis of Fig. 7. In Ref. [6], it has been shown through a one-dimensional simple man’s model that the energy separation between adjacent peaks will reach a maximum and then decrease with increasing photoelectron energy. It means that with increasing  $p_z$ , there will be more than one chance that the separations between adjacent fringes of the two interference processes become nearly the same, and so there would be more than one ringlike interference structure in the PAD.

In Fig. 8, we further show the TDSE simulation with Keldysh parameter  $\gamma = 0.28$  which is in the deep tunneling

regime. It can be seen that below  $p_z \sim 2$  a.u., there are several ringlike interference structures, which means that the direct and indirect electron trajectories play a dominant role in the PAD, and the interplay between the intra- and the intercycle interferences induces these ringlike patterns. These ringlike interference patterns blur the forklike holographic interference structure which can only be visible at larger  $p_z$ ’s. It should be noted that the holographic interference structure is indeed hardly distinguishable in recent experiments in the deep tunneling regime [20,21], which is consistent with our calculation. However, the ringlike interference structure may be smeared out by the focal average effect and therefore is also invisible in these experimental PADs.

#### IV. CONCLUSION

In conclusion, we have theoretically investigated 2D photoelectron momentum distributions in different Keldysh parameter regimes. We found that, in the deep tunneling regime, a profound ringlike interference pattern can be observed. We have identified that the ringlike interference pattern is induced by the interplay between the intra- and the intercycle interferences of electron trajectories. The center of the ringlike interference pattern lies in where separations between adjacent temporal double-slit interference fringes are nearly the same as those of the ATI fringes, which records electron dynamic information with attosecond subcycle resolution. The appearance of a ringlike interference pattern implies that the rescattered electrons play a negligible role. The holographic interference pattern can only be visible at larger  $p_z$ ’s where the contribution of the rescattered electrons can be discerned. In the nonadiabatic tunneling regime, the effect of the Coulomb potential will increase, so the contribution of the rescattered electron trajectories will increase, and the holographic interference pattern can clearly be distinguished. Our results indicate that the deep tunneling is not an appropriate condition for the observation of the holographic interference which is more clearly visible in the nonadiabatic tunneling regime.

#### ACKNOWLEDGMENTS

We benefited from discussions with X. Liu, W. Quan, and X. Xie. The work was supported by the National Key Program for S&T Research and Development (Grant No. 2016YFA0401100), the National Basic Research Program of China (Grant No. 2013CB922201), the National Natural Science Foundation of China (Grants No. 11374202, No. 11674209, No. 11274220, No. 11274050, No. 11334009, and No. 11425414), the Major Program of Guangdong Natural Science Foundation (Grant No. 2014A030311019), and the Open Fund of the State Key Laboratory of High Field Laser Physics (SIOM). W.Y. was supported by the “YangFan” Talent Project of Guangdong Province.

- [1] P. B. Corkum, *Phys. Rev. Lett.* **71**, 1994 (1993).  
 [2] L. V. Keldysh, *Sov. Phys. JETP* **20**, 1307 (1965).  
 [3] M. Y. Ivanov, M. Spanner, and O. Smirnova, *J. Mod. Opt.* **52**, 165 (2005).

- [4] F. Lindner, M. G. Schätzel, H. Walther, A. Baltuška, E. Goulielmakis, F. Krausz, D. B. Milošević, D. Bauer, W. Becker, and G. G. Paulus, *Phys. Rev. Lett.* **95**, 040401 (2005).  
 [5] R. Gopal *et al.*, *Phys. Rev. Lett.* **103**, 053001 (2009).

- [6] D. G. Arbó, K. L. Ishikawa, K. Schiessl, E. Persson, and J. Burgdörfer, *Phys. Rev. A* **81**, 021403(R) (2010).
- [7] D. G. Arbó, K. L. Ishikawa, K. Schiessl, E. Persson, and J. Burgdörfer, *Phys. Rev. A* **82**, 043426 (2010).
- [8] X. Xie, S. Roither, D. Kartashov, E. Persson, D. G. Arbó, L. Zhang, S. Gräfe, M. S. Schöffler, J. Burgdörfer, A. Baltuška, and M. Kitzler, *Phys. Rev. Lett.* **108**, 193004 (2012).
- [9] T. Remetter, P. Johnsson, J. Mauritsson, K. Varjú, Y. Ni, F. Lépine, E. Gustafsson, M. Kling, J. Khan, R. López-Martens, K. J. Schafer, M. J. J. Vrakking, and A. L'Huillier, *Nat. Phys.* **2**, 323 (2006).
- [10] Y. Huismans, A. Rouzée, A. Gijsbertsen, J. H. Jungmann, A. S. Smolkowska, P. S. W. M. Logman, F. Lépine, C. Cauchy, S. Zamith, T. Marchenko, J. M. Bakker, G. Berden, B. Redlich, A. F. G. van der Meer, H. G. Muller, W. Vermin, K. J. Schafer, M. Spanner, M. Y. Ivanov, O. Smirnova, D. Bauer, S. V. Popruzhenko, and M. J. J. Vrakking, *Science* **331**, 61 (2011).
- [11] T. Marchenko, Y. Huismans, K. J. Schafer, and M. J. J. Vrakking, *Phys. Rev. A* **84**, 053427 (2011).
- [12] D. D. Hichstein *et al.*, *Phys. Rev. Lett.* **109**, 073004 (2012).
- [13] W. Yang *et al.*, *Opt. Express* **22**, 2519 (2014).
- [14] M. Meckel *et al.*, *Nat. Phys.* **10**, 594 (2014).
- [15] X. Song, C. Lin, Z. Sheng, P. Liu, Z. Chen, W. Yang, S. Hu, C. D. Lin, and J. Chen, *Sci. Rep.* **6**, 28392 (2016).
- [16] M. G. Pullen *et al.*, *J. Phys. B* **47**, 204010 (2014).
- [17] C. I. Blaga *et al.*, *Nat. Phys.* **5**, 335 (2009).
- [18] W. Quan *et al.*, *Phys. Rev. Lett.* **103**, 093001 (2009).
- [19] C. Y. Wu, Y. D. Yang, Y. Q. Liu, Q. H. Gong, M. Wu, X. Liu, X. L. Hao, W. D. Li, X. T. He, and J. Chen, *Phys. Rev. Lett.* **109**, 043001 (2012).
- [20] J. Dura *et al.*, *Sci. Rep.* **3**, 2675 (2013).
- [21] B. Wolter *et al.*, *Phys. Rev. A* **90**, 063424 (2014).
- [22] M. Protopapas, C. H. Keitel, and P. L. Knight, *Rep. Prog. Phys.* **60**, 389 (1997).
- [23] M. J. Nandor, M. A. Walker, L. D. Van Woerkom, and H. G. Muller, *Phys. Rev. A* **60**, R1771(R) (1999).
- [24] X. M. Tong and S. I. Chu, *Chem. Phys.* **217**, 119 (1997).
- [25] W. Yang, X. Song, and Z. Chen, *Opt. Express* **20**, 12067 (2012).
- [26] W. Yang, X. Song, Z. Zeng, R. Li, and Z. Xu, *Opt. Express* **18**, 2558 (2010).
- [27] X. Tong, K. Hino, and N. Toshima, *Phys. Rev. A* **74**, 031405(R) (2006).
- [28] G. L. Yudin and M. Y. Ivanov, *Phys. Rev. A* **64**, 013409 (2001).
- [29] A. M. Perelomov, V. S. Popov, and M. V. Terent'ev, *Zh. Eksp. Teor. Fiz.* **50**, 1393 (1966) [*Sov. Phys. JETP* **23**, 924 (1966)].
- [30] T. Brabec, M. Y. Ivanov, and P. B. Corkum, *Phys. Rev. A* **54**, R2551(R) (1996).
- [31] B. Hu, J. Liu, and S. G. Chen, *Phys. Lett. A* **236**, 533 (1997).
- [32] J. Chen, J. Liu, and S. G. Chen, *Phys. Rev. A* **61**, 033402 (2000).
- [33] X. Wang, J. Tian, and J. H. Eberly, *Phys. Rev. Lett.* **110**, 243001 (2013).
- [34] P. Salières, B. Carrè, L. Le Dèroff *et al.*, *Science* **292**, 902 (2001).
- [35] M. Li, J.-W. Geng, H. Liu, Y. Deng, C. Wu, L.-Y. Peng, Q. Gong, and Y. Liu, *Phys. Rev. Lett.* **112**, 113002 (2014).
- [36] T.-M. Yan, S. V. Popruzhenko, and D. Bauer, in *Progress in Ultrafast Intense Laser Science*, edited by K. Yamanouchi and K. Midorikawa (Springer-Verlag, Heidelberg, 2013).